Tribol Lett (2011) 44:367–386
DOI 10.1007/s11249-011-9850-2

METHODS PAPER

Analytical Models for Atomic Friction

Yalin Dong · Ajay Vadakkepatt · Ashlie Martini

Received: 14 July 2011 / Accepted: 22 August 2011 / Published online: 17 September 2011

Abstract In this methods article, we describe application of Prandtl–Tomlinson models and their extensions to interpret dry atomic-scale friction. The goal is to provide a practical overview of how to use these models to study frictional phenomena. We begin with the fundamental equations and build on them step-by-step—from the simple quasistatic one-spring, one-mass model for predicting transitions between friction regimes to the two-dimensional and multi-atom models for describing the effect of contact area. The intention is to bridge the gap between theoretical analysis, numerical implementation, and predicted physical phenomena. In the process, we provide an introductory manual with example computer programs for newcomers to the field, and an illustration of the significant potential for this approach to yield new fundamental understanding of atomic-scale friction.

Keywords Nanotribology · Friction mechanisms · AFM · Stick-slip · Dynamic modeling

List of Symbols

Variables

a	Substrate lattice spacing
b	Tip lattice spacing
C_{eff}	Effective stiffness (cantilever, tip, and contact)
d	Superstructure periodicity
f	Actuation frequency
f_0	Attempt frequency
f_{nt}	Frequency of the tip apex mode (nanocontact)
f_{PT}	Frequency of the one effective mode of the PT model
F	Friction force
F_{c}	Maximum friction at zero temperature
F_{n}	Normal force
F_{ts}	Interaction force in the normal direction
k	System stiffness (cantilever and tip)
k_{t}	Stiffness of spring connecting neighboring tip atoms
k_{n}	Normal stiffness
m	Mass of tip
N	Number of atoms
p	Probability of a transition
t	Time
t_v	Average time for the tip to traverse one lattice spacing
T	Temperature
U	Corrugation potential amplitude
U_{c}	Corrugation potential
v	Sliding speed of support
v_{c}	Critical speed
V	Total potential energy
x	Displacement of the tip in the sliding direction
x_{t}	Transition point
x_{sp}	Displacement of the support
y	Displacement of the tip perpendicular to applied sliding direction
z	Displacement of the tip in the normal direction

Electronic supplementary material The online version of this article (doi:10.1007/s11249-011-9850-2) contains supplementary material, which is available to authorized users.

Y. Dong · A. Vadakkepatt
Purdue University, West Lafayette, IN 47907, USA

A. Martini (✉)
University of California Merced, Merced, CA 95343, USA
e-mail: amartini@ucmerced.edu

Greek Symbols

α Parameter that reflects the resonance of normal mode actuation
α_a Magnitude of amplitude modulation
α_c Magnitude of centerline modulation
β Curvature of the corrugation potential
γ Parameter that reflects the resonance of torsional mode actuation
η Stick-slip regime transition parameter
κ Transition rate
μ Viscous friction (damping) coefficient
ξ Thermal activation force
τ Average time to hop out from a potential well due to thermal activation
ω Angular frequency

1 Introduction

It has been proposed that fundamental insight into frictional phenomena might be gained by studying single asperity friction, where a single asperity is considered to be the basic element of friction on any length scale. The small size scale of a single asperity means that individual atoms may play a role in resisting motion, so single asperity friction is often called atomic-scale friction [1]. Atomic force microscopy (AFM) is the primary experimental tool used to investigate this phenomenon. To measure friction, the AFM cantilever gently drags a nanoscale sharp tip to slide against a substrate. The resulting interaction causes torsion of the cantilever which can be detected by optical techniques and then converted to a friction force. These friction measurements can also be understood using modeling and simulation.

Atomistic simulations such as molecular dynamics (MD) are popular and powerful tools to investigate atomic friction because they can track the evolution of each atom's configurational and energetic information. However, the cost of this level of detail is significant computation time. Further, atomistic simulations are limited in their ability to capture larger-scale features such as long times or large masses. An alternative is an analytical or reduced-order model that simplifies the system such that, while it cannot provide the level of detail of a fully atomistic simulation, it enables investigation of atomic friction under almost all experimental conditions (some of which are inaccessible to MD). Reduced-order models in this context refer to the Prandtl–Tomlinson (PT) model [2, 3] and its various extensions. This simple, yet widely used model consists of a harmonic spring that captures the combination of the stiffness of the tip and the first eigenmode of the cantilever torsion, and an equivalent point-mass that captures the effective mass corresponding to that eigenmode. Reduced-order, atomic-scale friction models simplify single asperity friction into one or more point-masses (contact area atoms) pulled via an elastic tether (compliant cantilever and tip) along a periodic potential energy profile (substrate).

There have been many modifications and extensions of the original PT model. One important extension is the introduction of thermal activation proposed by Gnecco et al. [4]. Other related methods are the Frenkel–Kontorova (FK) [5] and the Frenkel–Kontorova–Tomlinson (FKT) [6] models which take the size of the contact into consideration. The essential difference between the FK and FKT models is that only the end atom is attached to the support in FK while all atoms are attached to the support in FKT. The one-dimensional (1D) PT, FK, and FKT models are illustrated in Fig. 1. An advantage of all these models is that they can be easily implemented and enable the effects of individual parameters to be isolated to reveal fundamental mechanisms of atomic friction.

The goal of this article is to bridge the gap between theory and implementation of these models for studying atomic friction. For newcomers to the field, it can serve as an instructional tutorial; we have also provided example MATLAB programs in Supplementary Material to facilitate the learning process. The connection between fundamental concepts and their implementation provided in this

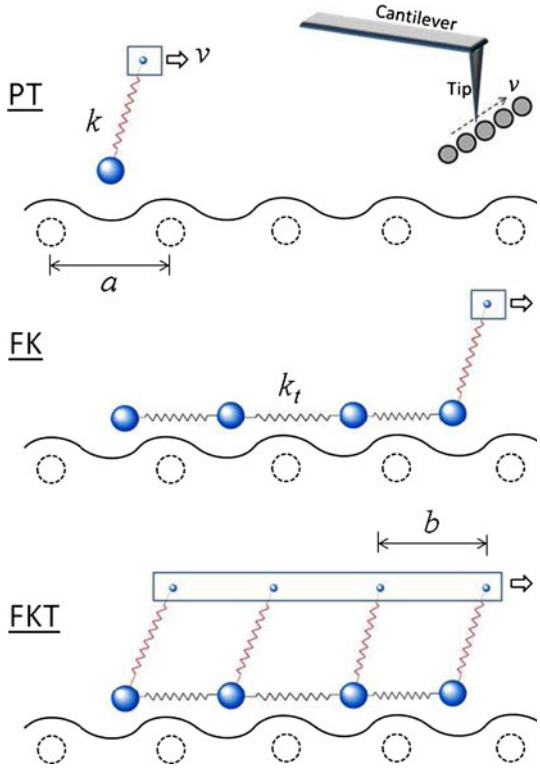

Fig. 1 Illustrations of the 1D PT, FK, and FKT models. *Large solid spheres* represent tip atoms and *rectangular slabs* represent the sliding support. *Inset* is a schematic of the relationship between an AFM tip/cantilever and the simple mass-spring model. Variables are defined in the text

article, in conjunction with the extensive literature cited, should provide researchers at all levels with an appreciation of how PT-based models can be used to gain fundamental insights into atomic-scale friction as well as the tools necessary to further this research direction.

We first introduce the basic mathematical formulation (Sect. 2) and describe how to implement robust numerical algorithms to solve the governing equations (Sect. 3). We then discuss application of PT-based models to describe thermal activation (Sect. 4), transitions between friction regimes (Sect. 5), friction modulation due to surface reconstruction (Sect. 6), dynamic actuation (Sect. 7), scan-line dependance (Sect. 8), and contact size effects (Sect. 9). The sections are organized by topic, and each section consists of a brief background on some frictional phenomenon and motivation for its study, details of how to extend and apply the PT model to describe that phenomenon, illustrative results predicted by the PT model, and finally suggestions for future research. References to the many studies that have contributed to progress in this area will be provided in the relevant sections.

2 Mathematical Formulation

The mathematical formulation of the reduced-order, atomic-scale friction models can be described using the 1D PT model as an example. The 1D PT model simplifies single asperity friction into a ball-like tip dragged to slide against the rigid substrate by a support moving at constant speed that is connected to the ball-like tip by a harmonic spring. The interaction between the tip and the substrate is modeled by a corrugation potential which has a sinusoidal form for a perfectly ordered crystalline surface. The total potential energy of the system $V(x, t)$ can be written as,

$$V(x,t) = -\frac{U}{2}\cos\left(\frac{2\pi x}{a}\right) + \frac{1}{2}k(vt - x)^2. \quad (1)$$

The first term on the right hand side of this expression describes the corrugation potential where U is the amplitude, x is the tip displacement, and a is the lattice spacing of the substrate. The second term is the elastic potential resulting from the interaction between the tip and support where k is the spring stiffness (or physically speaking the combined stiffness of the cantilever and tip), t is time, and v is the sliding speed of the support. The dynamics of the tip can be described by the Langevin equation,

$$m\ddot{x} + m\mu\dot{x} = -\frac{\partial V(x,t)}{\partial x} + \xi(t), \quad (2)$$

where m is the mass of the tip, μ is the viscous friction (or damping) coefficient, and $\xi(t)$ is the thermal activation force. This equation is solved for x and friction force is then calculated as

$$F = k(vt - x). \quad (3)$$

The governing equation of the PT model (Eq. 2) belongs to a family of stochastic differential equations composed of deterministic dynamics and stochastic processes. In this case, the deterministic term is a viscous drag to resist the movement of the tip and the force due to the corrugation potential in which the tip resides. The stochastic process is taken into consideration by adding a random force field $\xi(t)$, where $\xi(t)$ is a thermal noise term satisfying the fluctuation–dissipation relation,

$$\langle \xi(t)\xi(t') \rangle = 2m\mu k_B T\delta(t - t'). \quad (4)$$

In this expression, $\langle\ \rangle$ indicates an ensemble average, k_B is the Boltzmann constant, T is temperature, and δ is the Dirac delta function. With the stochastic term $\xi(t)$, given specific initial conditions, there is no deterministic path for the tip, i.e., multiple paths can be taken by the tip with specific probabilities.

Typical values and/or range of values for the parameters in these equations are given in Table 1. Note that this table only gives a general idea of the range of these parameters reported in the literature. The actual values used should be chosen on a case-by-case basis to correspond to the physical system being modeled. The exact values of parameters used in this article will be specified for each result presented. Also, it should be mentioned that the definition of mass is still controversial as will be discussed later. Finally, we want to point out that, although the Langevin equation is most common way to treat the thermal activation term, other methods exist, for example application of Monte Carlo methods [11, 12].

Table 1 Typical values or range of values for the parameters used in the PT model to describe an AFM friction experiment [7–10]

Variable	Magnitude
m, Mass of tip	10^{-12}kg
U, Amplitude of potential	1 eV
v, Sliding speed	1 nm/s–1 m/s
k, Cantilever and tip stiffness	0.1–50 N/m
a, Lattice spacing	0.3 nm
μ, Viscous coefficient	$2\sqrt{k/m}$
T, Temperature	0–1000 K

3 Numerical Algorithms

Ermak's algorithm [13, 14] to treat deterministic dynamics and stochastic processes simultaneously has been widely used to solve the governing equations of atomic friction [7,

9, 10, 15, 16]. The following describes the solution to a 1D Langevin equation; two-dimensional (2D) and three-dimensional (3D) solvers can be obtained in a similar manner. An example of this method is provided in the Supplementary Material as MATLAB program `PT1D_Ermak.m`. Based on Eq. 2, the discrete differential equations at each time step are,

$$\ddot{x}(t) = -\mu\dot{x}(t) - \frac{\partial V(x,t)}{m\partial x}, \tag{5}$$

$$\dot{x}(t+\delta t) = c_0\dot{x}(t) + c_1\delta t\ddot{x}(t) + \delta v^G, \tag{6}$$

$$x(t+\delta t) = x(t) + c_1\delta t\dot{x}(t) + c_2\delta t^2\ddot{x}(t) + \delta r^G, \tag{7}$$

where δt is the time step size. The parameters c_0, c_1, and c_2 are given by,

$$c_0 = \exp(-\mu\delta t), \tag{8}$$

$$c_1 = (\mu\delta t)^{-1}(1-c_0), \tag{9}$$

$$c_2 = (\mu\delta t)^{-1}(1-c_1) \tag{10}$$

The random variables δv^G and δr^G, which are used to describe the thermal activation term $\xi(t)$, can be sampled from a bivariate normal distribution. This distribution, ρ, is expressed,

$$\rho(\delta r^G, \delta v^G) = -\frac{1}{2\pi\sigma_r\sigma_v(1-c_{rv}^2)^{1/2}} \times \exp\left\{\frac{-1}{2(1-c_{rv}^2)}\left(\left(\frac{\delta r^G}{\sigma_r}\right)^2 + \left(\frac{\delta v^G}{\sigma_v}\right)^2 - 2c_{rv}\left(\frac{\delta r^G}{\sigma_r}\right)\left(\frac{\delta v^G}{\sigma_v}\right)\right)\right\} \tag{11}$$

where the mean values of the bivariate Gaussian distribution are zeros with variances given by,

$$\delta\sigma_r^2 = \delta t^2\frac{k_BT}{m}(\mu\delta t)^{-1} \times \left\{2-(\mu\delta t)^{-1}\left(3-4e^{-\mu\delta t}+e^{-2\mu\delta t}\right)\right\} \tag{12}$$

$$\delta\sigma_v^2 = \frac{k_BT}{m}\left(1-e^{-2\mu\delta t}\right) \tag{13}$$

and the correlation coefficient is,

$$c_{rv}\sigma_r\sigma_v = \delta t\frac{k_BT}{m}(\mu\delta t)^{-1}(1-e^{-\mu\delta t})^2. \tag{14}$$

Details for the derivation of c_0, c_1, c_2, δv^G, and δr^G can be found in the original papers [13, 14].

The one-step Ermak's algorithm is useful because it is straightforward and efficient, especially for computationally intensive systems such as those modeled using MD simulation containing thousands of atoms. The efficiency results from the low storage and the one-step method is crucial for many applications. However, the drawback of this algorithm is its first order accuracy which requires a short time step to obtain highly accurate results [17]. Alternatively, there are many higher-order algorithms that have been developed for stochastic differential equations [17–20]. Here, we introduce an implementation of the fourth-order Runge–Kutta (RK) algorithm developed by Kasdin [19]. While, other options are always available, we choose this method as an illustration for its performance and relatively easy implementation. An example of the fourth-order RK solution is provided in the Supplementary Material as MATLAB program `PT1D_RK.m`.

To implement this method, we separate the one variable equation with second order derivatives (Eq. 2) into two variable equations with first order derivatives.

$$\mathbf{X} = \mathbf{F}(\mathbf{X},t) + \Xi(t)$$
$$\overbrace{\begin{pmatrix}\dot{x}_1\\ \dot{x}_2\end{pmatrix}} = \overbrace{\begin{pmatrix}x_2\\ -\mu x_2 - \frac{1}{m}\frac{\partial V(x_1,t)}{\partial x_1}\end{pmatrix}} + \overbrace{\begin{pmatrix}0\\ \xi(t)/m\end{pmatrix}} \tag{15}$$

where $x_1 = x$ and $x_2 = \dot{x}$ are used to reduce the derivative order of the equation. Now, we can use vectors $\mathbf{X}$, $\mathbf{F}(\mathbf{X},t)$, and $\Xi(t)$ with two elements each to describe the variables of the equation sets.

Assuming that we know the value for $\mathbf{X}_k = \begin{pmatrix}x_1\\ x_2\end{pmatrix}$ at time step t_k, through fourth-step calculation (see equations below) we obtain the value for $\mathbf{X}_{k+1}$ at time t_{k+1}.

$$\begin{aligned}\mathbf{k}_1 &= \delta t\mathbf{F}(\mathbf{X}_k,t_k) + \delta tD^{1/2}\begin{pmatrix}0\\ r_1\end{pmatrix}\\ \mathbf{k}_j &= \delta t\mathbf{F}\left(\mathbf{X}_k + \sum_{i=1}^{j-1}a_{ji}\mathbf{k}_i, t_k + c_j\delta t\right) + \delta t(Dq_j)^{1/2}\begin{pmatrix}0\\ r_j\end{pmatrix}\\ \mathbf{X}_{k+1} &= \mathbf{X}_k + \alpha_1\mathbf{k}_1 + \ldots + \alpha_n\mathbf{k}_n\end{aligned} \tag{16}$$

where δt is the time step, $D = \frac{2m\mu k_BT}{\delta t}$, $j = 2\ldots n$, $n = 4$ for the fourth-order algorithm, and r is sampled by a standard Gaussian distribution with zero mean value and a variance of 1. The variables a_{ji}, α_i, and q_j are constant coefficients whose values are given in Table 2, and c is a constant that can be obtained by $c_j = \sum_{i=1}^{j-1}a_{ji}$. More details of the algorithm can be found in Kasdin's article [19].

Finally, we provide a case study to show successful applications of RK and Ermak's algorithm for thermal activation in atomic friction. The model-predicted friction at $T = 0$ and 300 K obtained from the two different algorithms is shown in Fig. 2. The results obtained using the two methods at 0 K are indistinguishable while there is clearly observable variation at 300 K where thermal

Table 2 Fourth-order, time-varying RK coefficients

Coefficient	Value
α_1	0.25001352164789
α_2	0.67428574806272
α_3	−0.00831795169360
α_4	0.08401868181222
a_{21}	0.66667754298442
a_{31}	0.63493935027993
a_{32}	0.00342761715422
a_{41}	− 2.32428921184321
a_{42}	2.69723745129487
a_{43}	0.29093673271592
q_1	3.99956364361748
q_2	1.64524970733585
q_3	1.59330355118722
q_4	0.26330006501868

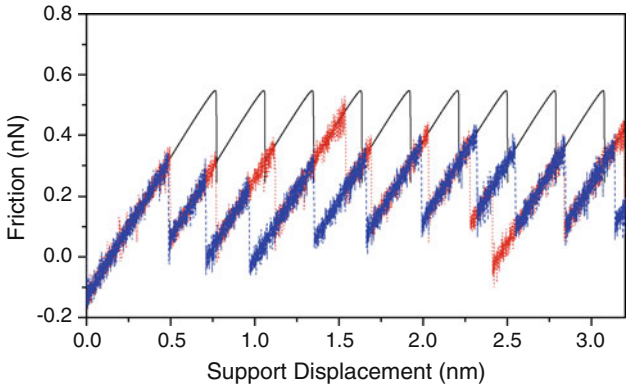

Fig. 2 Atomic friction versus support displacement at $T = 300$ K solved by the fourth-order RK algorithm (*dotted*) and Ermak's method (*dashed*). For reference, the friction at $T = 0$ K which is the same for both methods is also presented (*solid*). Other model parameters: $m = 10^{-12}$ kg, $k = 1$ N/m, $U = 0.6$ eV, $v = 4 \times 10^3$ nm/s, $\mu = 2\sqrt{k/m}$, $a = 0.288$ nm

activation is significant (discussed in a later section). Although, there is no standard with which the accuracy of the two methods predictions can be evaluated due to the stochastic nature of the problem, mathematical analysis has shown that the RK approach is generally more accurate [19]. Results reported in the remainder of this article are obtained using the fourth-order RK method.

4 Thermal Activation

The numerical methods introduced in the previous section are designed specifically to solve the problem of thermal activation. Generally speaking, when the energy barrier of a system comes close to the magnitude of $k_B T$ (0.026 eV at room temperature), thermal effects cannot be neglected. Therefore, in the case of a single nanoscale asperity contact with an energy barrier on the order of 1 eV, thermal effects are significant. A direct result of thermal activation—the contribution of thermal energy to overcome potential energy barriers—is a decrease of friction with temperature [7, 21] and an increase of friction with speed [4, 22–24].

In the PT model the total potential energy, consisting of the corrugation potential and elastic energy of the spring, evolves with time as the support moves with a constant speed ($x_{sp} = vt$). As shown in Fig. 3, this total energy defines the potential energy wells in which the tip may reside at a given time. If there is no thermal activation, the tip slips only when the energy barrier between the current potential well (i) and the adjacent potential well (j) disappears such that $\Delta V_{i\to j} = 0$. In the presence of thermal activation, the slip can occur sooner, i.e., when $\Delta V_{i\to j} > 0$. Provided that the sliding speed is slow enough, the transition rate, κ, for a jump from one potential well to next is given by,

$$\kappa = f_0 \exp(-\Delta V / k_B T), \tag{17}$$

where ΔV is the energy barrier that must be overcome for slip to occur, and f_0 is the attempt rate, the frequency at which the tip attempts to overcome a given energy barrier. The probability p_i of the tip residing at its current location relative to the corrugation potential is governed by,

$$\frac{\mathrm{d}p_i}{\mathrm{d}t} = -\kappa_{i\to j} p_i + \kappa_{j\to i} p_j. \tag{18}$$

This probability is related to the temperature, speed, and mass dependence of frictional behavior.

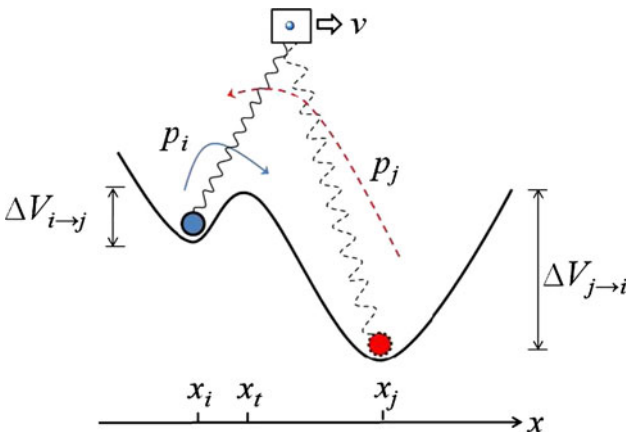

Fig. 3 An illustration of slip between two adjacent energy minima. p_i is the probability of the tip residing in the current potential well, i, where the energy barrier is $\Delta V_{i\to j}$. p_j is the probability of the tip residing at the next minima, j, where $\Delta V_{j\to i}$ is the corresponding energy barrier

4.1 Temperature

Figure 4 shows the effect of temperature on mean friction and illustrates that there are two regimes of temperature dependance, thermal activation, and thermal drift. Representative force traces in these two regimes are given in Fig. 5. At lower temperatures, the system is subject to standard thermal activation where we suppose $\Delta V_{j\to i} \gg \Delta V_{i\to j}$ so that $\kappa_{j\to i} \ll \kappa_{i\to j}$, the adsorbed boundary condition (no backward slip) is employed, and then

$$\frac{\mathrm{d}p_i}{\mathrm{d}t} = -\kappa_{i\to j} p_i. \tag{19}$$

In this case, the relationship between friction, temperature, and speed follows Sang et al.'s prediction [7],

$$F = F_\mathrm{c} - |\beta k_\mathrm{B} T \ln\left(\frac{v_\mathrm{c}}{v}\right)|^{2/3}, \tag{20}$$

where F_c is the maximum friction at $T = 0$, $v_\mathrm{c} = \frac{2f_0\beta k_\mathrm{B}T}{3C_\mathrm{eff}\sqrt{F_\mathrm{c}}}$ is the critical velocity, f_0 is the attempt rate, C_eff is the effective stiffness, and β is a parameter determined by the shape of the corrugation potential. Equation 20 characterizes the thermal activation regime which exhibits a rapid decrease of friction (low temperatures in Fig. 4) and persistent forward slip (top plot of Fig. 5). Assuming a sinusoidal potential corrugation, an analytical expression for the corrugation potential shape can be derived [21], $\beta = (3\pi\sqrt{F_\mathrm{c}}/(2\sqrt{2}a)$. A more detailed discussion of β for different forms of the corrugation potential has also been presented [25]. Note that C_eff differs from k, in that k describes the stiffness of the cantilever and tip, while C_eff includes the contact stiffness as well as the cantilever and tip stiffness. The magnitude of C_eff can be determined from the slope of the friction versus support displacement curve.

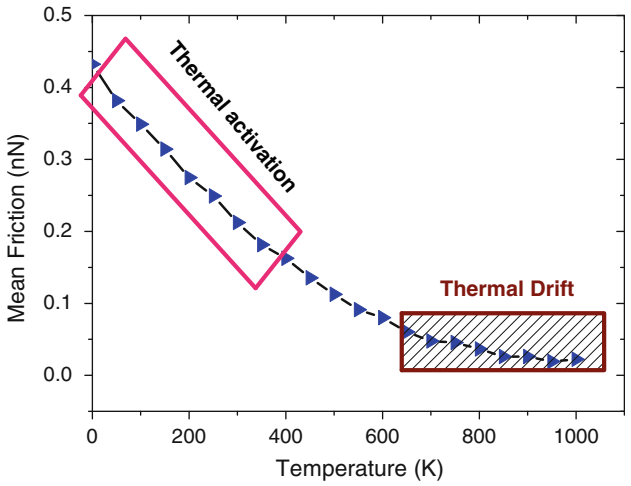

Fig. 4 Illustration of the temperature dependence of friction. The two regimes identified on the plot, thermal activation and thermal drift, are described in the text. Other model parameters: $m = 10^{-12}$ kg, $U = 0.6$ eV, $v = 4 \times 10^3$ nm/s, $\mu = 2\sqrt{k/m}$, $a = 0.288$ nm

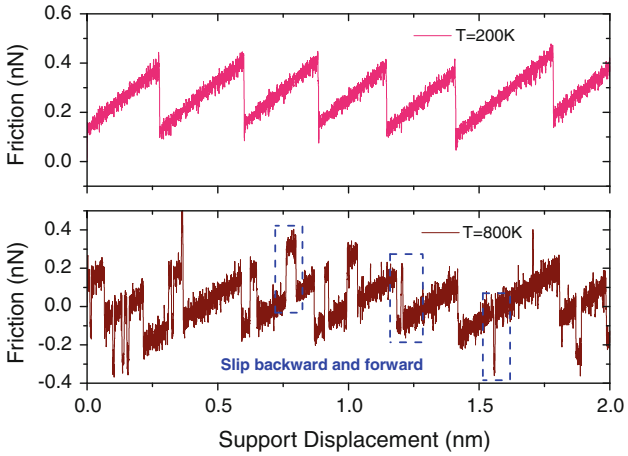

Fig. 5 Representative force traces in the thermal activation (*top*) and thermal drift (*bottom*) regimes identified in Fig. 4. Several characteristic forward and backward slips are identified by *dashed lines* on the friction trace in the thermal drift regime

When the temperature is high enough that the system is consistently close to thermal equilibrium, the system enters the thermal drift regime [26]. The transition between regimes can be understood by considering two time scales. First is the average time for the tip to traverse over one lattice spacing, $t_v = a/v$. Second is the average time for the tip to hop out from the potential well with the assistance of thermal activation,

$$\tau = 1/\kappa = \frac{1}{f_0}\exp\left(\frac{\Delta V}{k_\mathrm{B}T}\right). \tag{21}$$

If $t_v \gg \tau$, then the system is in the thermal drift regime where friction follows the prediction of Krylov et al. [11, 26, 27],

$$F \propto \frac{v}{T}\exp(1/T). \tag{22}$$

In the thermal drift regime, the system exhibits consistently low mean friction (high temperatures in Fig. 4) with both forward and backward slips (bottom plot of Fig. 5).

It is now widely accepted that thermal activation of the tip in overcoming an energy barrier can lead to a monotonic decrease of friction as discussed above. However, experiments on MoS_2 [28] and silicon wafers [29] reveal that there can be an increase in friction with temperature before the friction force declines rapidly (sometimes called a friction peak). An interpretation of the friction peak was proposed by Barel et al. [30] who argued that, in addition to thermal activation from the energy barrier, there also exist thermally activated formation and rupturing of multiple contacts, the competition between which can explain the force peak. An enhanced PT model incorporating the

effect of multiple contacts was successfully applied to phenomenologically verify this mechanism [30, 31]. This effect cannot be captured by a single contact PT model such as that used in this article, so no force peak is observed in the results presented here.

4.2 Speed

Figure 6 shows the speed dependence of friction. At low speeds, the relationship follows Sang et al.'s prediction (Eq. 20), that friction scales logarithmically with speed. Based on this prediction, when $v > v_c$, if only thermal effects are considered, the friction will saturate (sometimes called a friction plateau) and no longer increase with additional increases in speed [23]. An analytical prediction of the appearance of the friction plateau (the mean friction $F_c = 0.39$ nN at T = 0 K) is shown as a dashed line in Fig. 6. However, in the reduced-order model, as the speed goes up the system enters an athermal regime where the thermal effects are negligible compared to other contributions [32]. In the athermal regime the damping term, $v\sqrt{mk}$, dominates the process and the friction is proportional to velocity, $F \propto v$. The athermal region is often observed in the reduced-order model if the system is overdamped or at high scanning speed. The appearance of the athermal regime can hinder the observation of a friction plateau [8] which explains why there is no obvious friction plateau in the results shown here. These findings also suggest that special attention is needed for interpretation of MD simulation results due to the fact that the speeds accessible to the simulation often fall into the athermal regime [24].

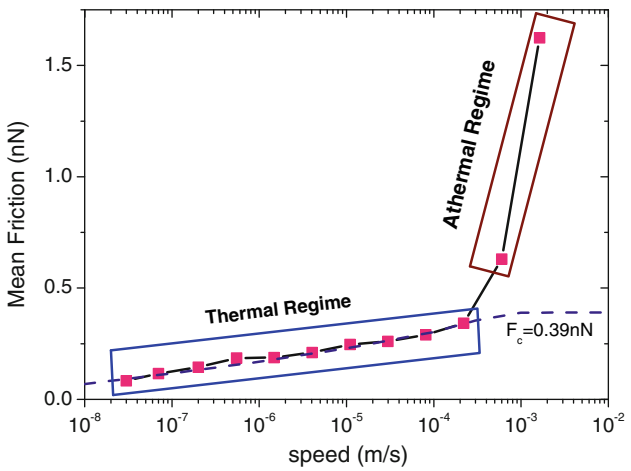

Fig. 6 Speed dependence of friction illustrating two different regimes. In the thermal regime, there is a logarithmic scaling of friction with speed, and in the athermal regime the friction is governed by the damping term such that $F \propto v$. The friction plateau ($F_c = 0.39$ nN) predicted by thermal activation is identified by the *dashed line*. Other model parameters: $m = 10^{-12}$ kg, $U = 0.6$ eV, $T = 300$ K, $v = 4 \times 10^3$ nm/s, $\mu = 2\sqrt{k/m}$, $a = 0.288$ nm

It is still unclear to what extent athermal effects play a role for real dynamical systems in which there exist many dissipation channels instead of a single viscous term [33]. It is also worth pointing out that, although majority of AFM experiments and simulations predict an increasing friction with velocity, the monotonic relation is not always measured. For example a non-monotonic velocity dependence of friction has been experimentally observed under some conditions [34] and theoretically predicted by taking other mechanisms such as memory effects or substrate dissipation into account [35–37].

4.3 Mass

One may note that there is an important parameter arising in the equations describing thermal activation that has not yet been discussed, the attempt rate f_0. Following Kramer's rate theory [38], f_0 can be expressed as,

$$f_0 = \left(\left(\frac{\mu^2}{4} + \omega_t^2\right)^{1/2} - \frac{\mu}{2}\right)\frac{\omega_i}{2\pi\omega_t} \tag{23}$$

where μ is the viscous friction coefficient, $\omega_i^2 = m^{-1}V''(x_i)$ is the squared angular frequency at the metastable minimum i, and $\omega_t^2 = m^{-1}V''(x_t)$ denotes the squared angular frequency at the transition point. In the extreme situation of an overdamped system where $\mu \gg \omega_t$, the attempt frequency becomes,

$$f_0 = \frac{\omega_i\omega_t}{2\pi\mu}. \tag{24}$$

Or for a system without damping where $\mu = 0$, the attempt rate reduces to,

$$f_0 = \frac{\omega_i}{2\pi}. \tag{25}$$

For this case, an expression relating the attempt rate f_0 to mass m and stiffness k can be deduced analytically, $f_0 = \frac{1}{2\pi}\sqrt{\frac{2\pi^2 U}{ma^2}\cos\left(\frac{2\pi x_i}{a}\right) + \frac{k}{m}}$. In general though, the attempt rate increases with stiffness and decreases with mass regardless of the state of damping in the system.

Figure 7 demonstrates the effect of mass, or equivalently the system's inertia, on its frictional temperature and speed dependence. A smaller inertia (larger attempt rate) causes an earlier transition (i.e., at lower temperature) into the thermal drift regime, where the transition is determined by the criteria in Eq. 21. Smaller inertia also leads to later saturation of the speed dependence and so a later transition

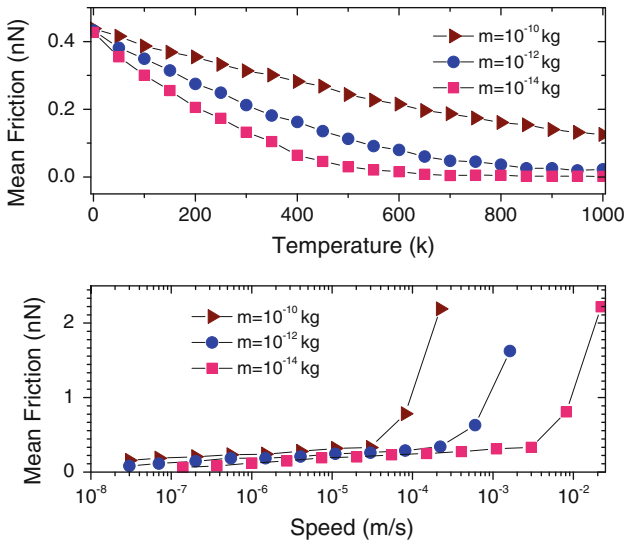

Fig. 7 The effect of tip mass (inertia) on the temperature and speed dependence of friction. Other model parameters: $U = 0.6\,\text{eV}$, $\mu = 2\sqrt{k/m}$, $a = 0.288\,\text{nm}$

(i.e., at larger speed) to the athermal regime. The later transition to the athermal regime can be rationalized by the observation that athermal friction is determined by $F = v\sqrt{mk}$ (at large v the term $m\mu\dot{x}$ dominates Eq. 2), so the smaller the effective tip mass the later the athermal regime arises.

In principle, f_0 can be tuned by varying k, the stiffness of cantilever and tip, or m, the effective mass. This brings up the issue of how to define mass. Traditionally, PT-based models consider the entire mass of the tip which is the order of 10^{-12} kg. However, it has been suggested that elastic deformation could be localized at the apex of the tip for which the inertia is much less than the typically used value [39]. This smaller mass causes a significant increase in the attempt rate of the system, and therefore leads to prediction of a stronger thermal effect. One means of addressing this issue is to separate the mass of the tip apex from that of the body of the tip and the cantilever by using a two-mass, two-spring model. Such a model can provide a better description of the tip's flexibility [11, 39–43]. However, it still does not resolve the issue of how to differentiate the tip apex from the whole, or how to determine the mass of the tip apex. Despite these issues, it is clear that the system's inertia affects predictions of thermal effects made using the PT model. The significance of this effect was recently shown by Li et al. [24] through optimally matched experiments and MD simulations where the large discrepancy between the mass of the model and experimental tips resulted in a significant difference between the measured and predicted frictional behavior.

5 Friction Regimes: Smooth Sliding, Single Slip, and Multiple Slip

Atomic friction can be divided into different regimes: smooth sliding where the AFM tip slides smoothly on the substrate, single slip where the tip sticks at one point and then jumps over one lattice spacing to another point, and multiple slip where the tip jumps over a few (more than one) lattice spacings. Stick-slip motion is a very important instability mechanism and is associated with high friction and energy dissipation. Finding ways to control transitions from smooth sliding to stick-slip has been thought to be a key to prescribing friction at the atomic scale. Considering the importance of transitions between friction regimes, it is relevant to understand the underlying mechanisms. In principle, the parameters that influence friction regimes fall into two categories, static and dynamic.

If we view sliding friction as a quasistatic process, temperature, sliding speed, and damping can be neglected. With this assumption, Eq. 1 can be simplified as $\frac{\partial V(x,t)}{\partial x} = 0$, to find the balance position for the tip, or equivalently, the number of potential energy minima available. Therefore, the 1D static PT model is described by the equation,

$$\frac{\pi U}{a}\sin\left(\frac{2\pi x}{a}\right) = k(x_{\text{sp}} - x) \tag{26}$$

where x_{sp} is the support position. The friction regime is determined by how many solutions this equation has: one solution corresponds to smooth sliding, two solutions to single slip, three solution to double slip, and so on. Based on this, it has been found that transitions between friction regimes can be characterized by the parameter $\eta = \frac{2\pi^2 U}{a^2 k}$, where the critical values of $\eta = 1$, 4.6, 7.79, and 10.95 are associated with transitions to single, double, triple, and quadruple slips, respectively. The prediction of these critical values was proposed by Johnson et al. [44] and codified by Medyanik et al. [45].

Figure 8 illustrates the total potential energy at different values of η. This figure shows that, for $\eta \leq 1$, a single potential minima exists downhill from the tip's current position and therefore only smooth sliding can occur. At $1 < \eta \leq 4.6$, two potential minima exist and so it is possible for the tip to traverse from one energy minima to the next; in other words a single slip could occur. Similarly, $(n-1)$ fold slip could occur only when n potential minima exist. So for a quasistatic system, the parameter $\eta = \frac{2\pi^2 U}{a^2 k}$ can independently determine transitions between friction regimes.

The critical values of η derived from statics determine the probability of the occurrence of slip; however, it is dynamics that ultimately determine transitions between friction regimes [33]. The first dynamic parameter we

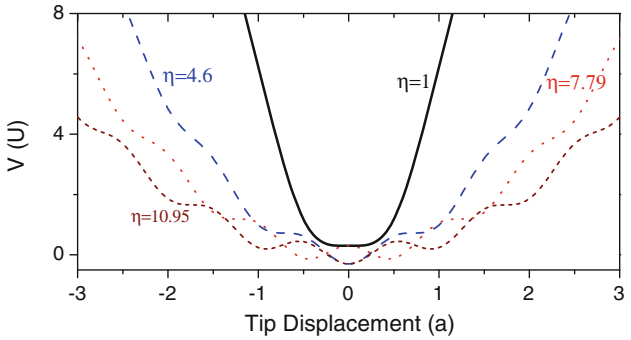

Fig. 8 Illustration of potential energy with varying number of energy minima for different values of the transition parameter η

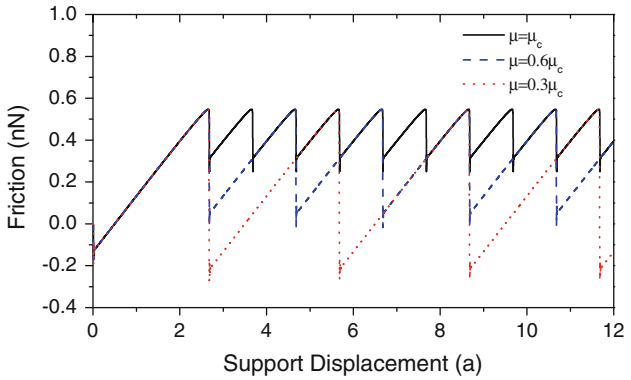

Fig. 9 The effect of damping on transitions between slip regimes where $\mu_c = 2\sqrt{k/m}$ is the critical damping coefficient. Single, double, and triple slip occur at $\mu = \mu_c$, 0.6 μ_c, and 0.3 μ_c, respectively. The abscissa has units of the lattice spacing a to facilitate identification of the transitions between single, double, and triple regimes. Other model parameters: $U = 0.6$ eV, $T = 0$ K, $v = 1$ μm/s, $m = 10^{-12}$ kg, $k = 1$ N/m, $a = 0.288$ nm

consider is damping. In the extreme condition where damping is very strong, i.e., the rate of transfer of kinetic energy to heat is much larger than the energy associated with slip, the system can only jump from the current minima to an adjacent one, and thus only single slip can occur. This suggests that damping can delay the occurrence of multiple slip. Figure 9 demonstrates the effect of damping on transitions between slip regimes; a decrease in the damping coefficient μ causes transitions from single to double and then triple slip. Direct measurement of the damping coefficient in an AFM contact is difficult [46] and requires continuum-based assumptions about the relationship between contact area and normal load which have been argued to be invalid [47]. However, by observing the relation between damping and slips, Roth et al. have proposed to use the occurrence of multiple slip as an indicator for AFM damping through the relationship between damping and slip [46].

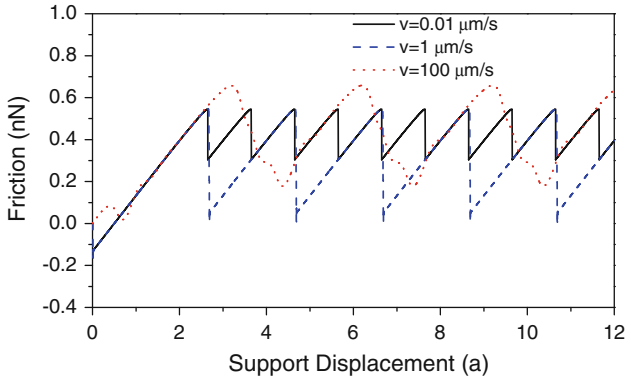

Fig. 10 The effect of sliding speed on transitions between slip regimes. Single, double, and triple slip occur at $v = 100$, 1, and 0.01 μm/s, respectively. Other model parameters: $U = 0.6$ eV, $T = 0$ K, $\mu = 0.8\ \mu_c$, $m = 10^{-12}$ kg, $k = 1$ N/m, $a = 0.288$ nm

Another dynamical factor is sliding speed. Figure 10 illustrates that the sliding speed can encourage transitions between friction regimes; that is, increasing speed is associated with multiple slips. The mechanism underlying this trend can been understood easily in terms of energetics since at higher speeds the tip has more kinetic energy to transverse over additional potential energy barriers [15]. At finite temperatures, a higher sliding speed can also lead to later slip through thermal activation. The slip occurs close to the transition point and the potential energy stored in the cantilever at the onset of slip is large, leading to a larger proportion of multiple slips [33]. One may also notice from Fig. 10 that at $v = 100$ μm/s the maximum friction increases. That is because at high speeds the viscous term starts to dominate the process and the system enters the athermal regime as discussed previously.

The last dynamical factor in the PT model we will consider is temperature. Without temperature effects, slip only occurs when there is no longer an energy barrier to escape the potential minima where the tip resides. Temperature can trigger the occurrence of slip at an earlier stage through thermal activation. The jump at an earlier stage through thermal activation will result in not only less potential energy accumulated and so less kinetic energy transferred, but also fewer potential minima available downhill [33]. Therefore, the higher the temperature, the less probability of multiple slip. This effect is illustrated in Fig. 11.

These types of observations can be exploited as potential means of controlling friction by, for example, manipulating the amplitude of the corrugation potential U. Some attempts have already been made: Socoliuc et al. achieved transitions between friction regimes by tuning the normal load [48] and Dienwiebel et al. realized similar transitions by controlling the commensurability between tip and substrate [49]. However, further investigation of the parameters that affect

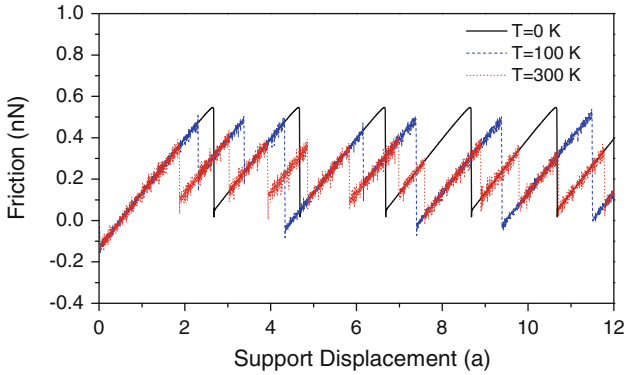

Fig. 11 The effect of temperature on transitions between slip regimes. Other model parameters: $U = 0.6$ eV, $v = 1$ μm/s, $\mu = 0.6\ \mu_c$, $m = 10^{-12}$ kg, $k = 1$ N/m, $a = 0.288$ nm

transitions between friction regimes using reduced-order models may yield even more novel ideas for friction control.

6 Friction Modulation Due to Surface Reconstruction

So far, we have only considered friction on an atomically flat, defect-free surface. However, many surfaces are non-ideal and exhibit defects, disorder, or reconstruction that result in corresponding variation in friction. In this section, we focus on reconstruction, which refers to a scenario where atoms near a surface reside in positions different from the bulk material and form a new "reconstructed" surface, sometimes called a "superstructure". One representative and well-known example is Au(111) surface reconstruction [50, 51].

Friction variation due to reconstruction was recently observed with KBr films formed on NaCl(001) and Cu(111) surfaces [52]. In that study, friction as well as energy dissipation were found to vary with the reconstructed surface features, and these observations were attributed to a tiny rumpling in the direction perpendicular to the surface on the order of 0.01 nm. Recently, a graphene film on SiC(0001) with 6 × 6 reconstruction was also found to give rise to friction modulation. However, in that case there was no variation in the energy dissipated because the offsets of the force trace and retrace were consistent [53]. These and other results suggest that it may be feasible for friction to be controlled at the nanoscale by utilizing topographic features provided by different superstructures.

For an ideal clean crystal surface, the PT model corrugation potential can be represented by a sinusoidal form. However, this simple approach cannot capture atomic disorder. Friction on non-ideal surfaces has been investigated in the framework of the PT model by introducing a local perturbation [54] or including a second harmonic term [55]. Instead of modifying the sinusoidal potential to capture surfaces features, friction modulation has also been studied using a non-sinusoidal potential [25, 56]. To show the application of reduced-order modeling to study surface reconstruction, we follow Steiner et al. [57] and employ a 1D PT model at $T = 0$ K to phenomenologically interpret the friction modulation.

To capture the presence of a superstructure on a substrate surface, the PT corrugation potential must be modified correspondingly. As suggested by Steiner et al. [57], two types of modulation could exist. The first is called amplitude (or friction loop width) modulation where a long range modulation is applied to the amplitude of the corrugation potential. The modulated corrugation potential can be written as,

$$U_c(x) = \frac{1}{2}U\left[1 + \alpha_a \cos\left(\frac{2\pi x}{d}\right)\right]\cos\left(\frac{2\pi x}{a}\right), \tag{27}$$

where U is the amplitude of the corrugation potential before modulation, α_a is an artificial parameter used to adjust the magnitude of the modulation, and d is the periodicity of the superstructure. Figure 12 shows the form of the corrugation potential after amplitude modulation with the corresponding model-predicted force trace and retrace depicted below. If one views the energy dissipation as the area confined between force trace and retrace, the energy dissipation is largest at the point where the amplitude of corrugation potential is a maximum while there is almost no energy loss elsewhere. Therefore, in amplitude modulation, both the force and energy vary due to the underlying superstructure. This is consistent with the experimental measurements of films formed by KBr on NaCl(001) and Cu (001) [52].

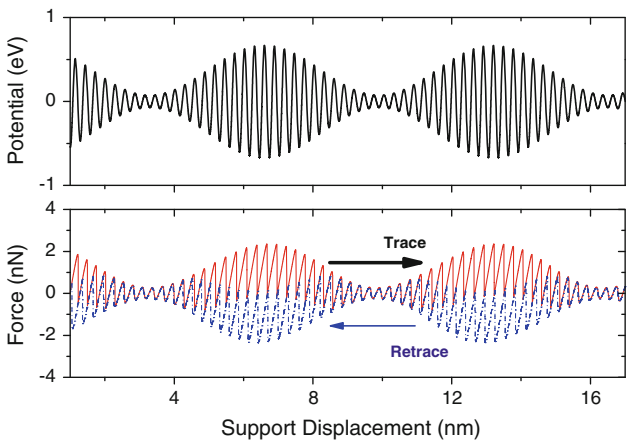

Fig. 12 Amplitude (friction loop width) modulation induced by multiplying the sinusoidal corrugation potential by a long-range modulation term (*top*) and the resulting force trace (*solid*) and retrace (*dashed*) predicted by the PT model (*bottom*); $T = 0$ K

Another illustration of this effect is called centerline (or friction loop offset) modulation. This phenomena is incorporated into the PT model by adding a long range potential to the short range sinusoidal potential,

$$U_c(x) = \frac{1}{2}U\cos\left(\frac{2\pi x}{a}\right) + \frac{1}{2}U\alpha_c\cos\left(\frac{2\pi x}{d}\right), \quad (28)$$

where α_c describes the magnitude of the centerline modulation. Figure 13 demonstrates the modulated potential form and the resultant model-predicted force trace and retrace. In contrast to amplitude modulation, the force trace and retrace are modulated consistently such that there is almost no variation of the energy dissipation. Similar friction force traces with centerline offset modulation have been acquired on graphene films grown on SiC(0001) [53].

Both of types of friction modulation observed in experiments can be captured by the PT model with a modulated corrugation potential. However, this does not directly answer the question of where the modulated potential comes from. Initial work has been done by Li et al. [58] to explain the friction offset modulation on a reconstructed Au (111) surface using MD simulation. The fully atomistic model revealed that the cause of the friction modulation is *not* the tiny rumpling in the normal direction, but rather can be attributed to the transitions from face-centered-cubic (FCC) to hexagonal-close-packed (HCP) structure on the surface. However, there is still a significant gap between observation of friction modulation and having sufficient understanding of the fundamental mechanisms to enable use of surface reconstruction as a means of controlling friction which invites further investigation.

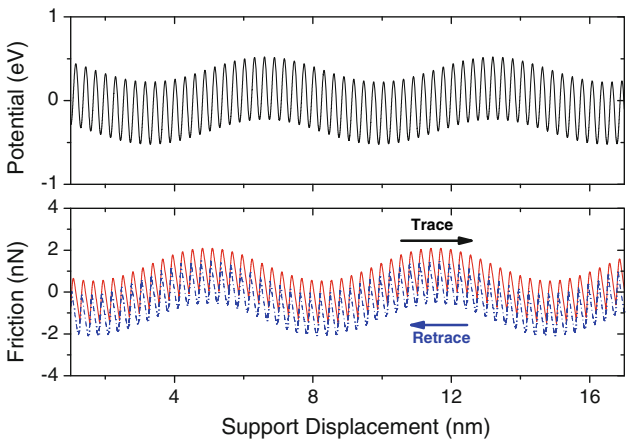

Fig. 13 Centerline (friction loop offset) modulation induced by adding the sinusoidal corrugation potential to a long-range modulation term (*top*) and the resulting force trace (*solid*) and retrace (*dashed*) predicted by the PT model (*bottom*); $T = 0$ K

7 Dynamic Actuation

It has been reported that friction at the nanoscale can be drastically decreased by mechanically exciting the normal [59] or torsional [23] modes of an AFM cantilever. These two approaches are illustrated schematically in Fig. 14. The idea of controlling friction by driving an AFM near its resonance frequency originates from the invention of dynamic mode AFM which, in contrast to contact mode, has the advantage of causing less wear and can provide more information such as phase, frequency, amplitude, and so on. For example, Lantz et al. showed that the dynamic mode can substantially decrease wear during the sliding of an ultrasharp silicon tip against a polymer surface [60], which gives promise to new technologies for applying nanoprobes to read and write data. In this section, we focus on how to simplify this complicated system into a reduced-order model, and demonstrate how to employ such a model to facilitate understand the physical phenomena.

In Socoliuc et al.'s [59] study, excitation is achieved through modulation of the normal force acting on the tip at well-defined frequencies. Then the movement of the tip in the normal direction is governed by the equation,

$$m\ddot{z} + c\dot{z} + k_n z = F_{ts}(z) + F_{n0}\cos(2\pi f t) \quad (29)$$

where z is the displacement in the normal direction, $c\dot{z}$ is the dissipation term, k_n is the normal stiffness of the system, F_{ts} is the interaction force in the normal direction between the tip and substrate, and F_{n0} is the magnitude of the normal force (F_n) exerted on the system.

The steady state solution of this problem can be written as,

$$z(t) = Z_0\cos(2\pi f t - \phi), \quad (30)$$

where the tip will oscillate with the same frequency f but with a phase lag ϕ, and amplitude Z_0 which is determined by the quality factor and the excitation frequency. When f coincides with the characteristic frequency of the system, resonance occurs such that Z_0 reaches its maximal value. The characteristic frequency of the system is determined by

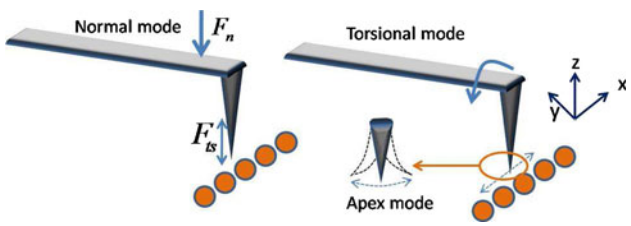

Fig. 14 Characteristic vibrational modes of the micro-cantilever. The normal mode that can be excited by a mechanical modulation of the normal force, the torsional mode that can be excited by a mechanical modulation of torsion. F_n is the normal force and F_{ts} is the interaction force between tip and substrate

the normal stiffness k_n, effective mass m, and the interaction force F_{ts}, and so is usually larger than that of a free system without F_{ts} [23, 61].

The variation of z can be implicitly reflected in the PT model by variation of the magnitude of the corrugation potential U. An approximation is to suppose that U varies linearly with z, so the variation of the magnitude of the corrugation potential also has a harmonic form [16, 59],

$$U = U_0[1 + \alpha\cos(2\pi ft)] \tag{31}$$

where α is used to reflect the magnitude of z.

Another approach is to excite the torsional mode of the system [23, 62]. The excitation of the torsional mode leads to an oscillating motion of the tip in the sliding direction. In this case, the speed of the tip has the form,

$$v = v_0[1 + \gamma 2\pi fa\cos(2\pi ft)] \tag{32}$$

where v_0 is the constant sliding speed without excitation, a is the lattice spacing in the sliding direction, and γ is used to describe the oscillation strength. In practice, γ can be controlled by adjusting f; when f is equal to the characteristic torsional mode of the system, γ reaches its maximum value. Note that U and v in Eqs. 31 and 32 are the magnitude of the corrugation potential and sliding speed in Eq. 1.

The dependence of friction on α, the parameter that reflects the resonance of the normal mode, and γ, the parameter that reflects the resonance of the torsional mode, are demonstrated in Figs. 15 and 16. It is clear that both excitations can decrease the atomic friction significantly. Recall that a small value of α or γ represents the scenario where the excitation frequency is far from the characteristic

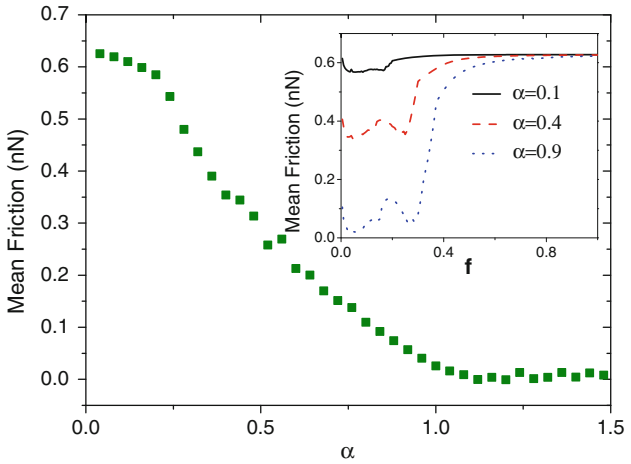

Fig. 15 Friction dependence on α, the parameter that describes actuation of the normal mode of an AFM system. *Inset* is the variation of friction with excitation frequency (units $\sqrt{\frac{k}{m}}$) for different α. Other model parameters: $m = 10^{-12}$ kg, $U_0 = 1.2$ eV, $v = 1 \times 10^3$ nm/s, $\mu = 2\sqrt{k/m}$, $a = 0.288$ nm, $k = 4$ N/m and $T = 0$ K

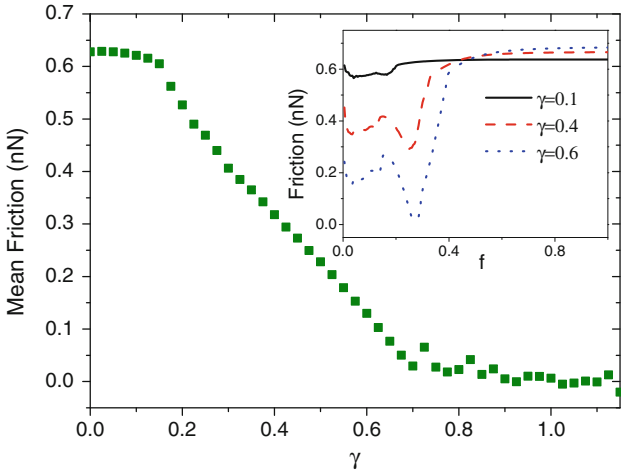

Fig. 16 Friction dependence on γ, the parameter that captures actuation of the torsional mode of an AFM system. *Inset* is the variation of friction with excitation frequency (units $\sqrt{\frac{k}{m}}$) for different γ. Other model parameters: $m = 10^{-12}$ kg, $U = 1.2$ eV, $v_0 = 1 \times 10^3$ nm/s, $\mu = 2\sqrt{k/m}$, $a = 0.288$ nm, $k = 4$ N/m and $T = 0$ K

frequency of the system, while large α or γ corresponds to the occurrence of resonances.

According to Socoliuc et al. [59] the actuation frequency, f, must satisfy the following criteria,

$$v/a \ll f \ll f_{nt} \tag{33}$$

where v/a is the frequency that the tip traverses over a lattice spacing of the substrate and f_{nt} is the frequency of the nanocontact which is related to the fast motion of the tip apex. However, in the simplified PT model there is just one-spring and one point-mass, so we can represent only one effective mode, i.e., the combination of the tip apex and cantilever, the frequency of which is f_{PT}. For a system without damping, the frequency of the PT mode can be defined as,

$$f_{PT} = \frac{\sqrt{V''(x)/m}}{2\pi}, \tag{34}$$

where V is the total system potential and x represents the slip position of the nanocontact. For α or $\gamma = 0$ and at zero temperature, the slip occurs at the saddle point of the total potential where $V''(\frac{2\pi x}{a}) = 0$, so f_{PT} becomes zero. When α or γ increases, the slip occurs at an earlier stage and a larger V'', thus the resonance occurs at a larger f_{PT}.

In the reduced-order model, we can vary the excitation frequency f easily and investigate its effect on friction. From the insets of both Figs. 15 and 16, we can see that there are two local friction minima. The first minimum occurs when the frequency is equal to v/a. This minimum friction is caused by resonance between the traversing frequency v/a and the external excitation frequency f. The location of the first minimum is the same for all curves in

the insets since the same sliding speeds are applied. The second minimum arises when the external excitation frequency is identical to that of the PT mode, f_{PT}, which depends on the slip position. So this minimum friction is due to resonance between the frequency of the PT mode and the external exciting frequency. As shown in the insets of Figs. 15 and 16, an increase in α or γ results in a slight shift of the second minima to the right. When the external excitation frequency is not contained between v/a and f_{PT}, the suppression of friction will not occur.

In practice, the typical frequency of the 1st normal eigenmode or 1st torsional eigenmode (on the order of 100 kHz) is much smaller than that of apex mode f_{nt} (on the order of GHz), and is much larger than the traversing frequency v/a (on the order of kHz assuming a scanning speed of 1μm/s and lattice spacing at 0.5 nm). So, in general the excitation frequency is well contained between v/a and f_{nt}. However, we do not exclude the cases where the higher eigenmodes of the microcantilever are excited or the scanning speed is on the order of mm/s or m/s which is common in MD simulation.

8 2D Nature of Atomic Friction

There is a significant limitation in the PT model we have discussed so far in that the trajectory of the tip is limited to one dimension. In reality, the tip may move in two dimensions. Fujisawa et al. [63] experimentally revealed that atomic friction exhibits remarkable 2D behavior. Subsequent study [64, 65] confirmed that this phenomenon is ubiquitous on atomically flat surfaces. This means that the AFM tip usually takes a 2D trajectory instead of a straight line path while sliding along an atomically flat surface. Because of this, atomic friction exhibits many unique phenomena such as dependence on the scanning direction and the scanning line. An extended version of the PT model has been successfully used to predict the 2D nature of atomic friction [10, 66, 67]. In this section, we will show (a) how to construct a 2D corrugation potential and (b) application of the 2D PT model to study the scan-line dependance of friction. An example implementation of the 2D PT model is provided in the Supplementary Material as MATLAB program `PT2D_RK.m`.

8.1 2D Corrugation Potential

In the 2D PT model, a tip composed of a single atom slides along an energy landscape that models a 2D lattice of atoms. For different lattice structures, one has to construct corresponding formulas for the energy landscape. Most material surfaces fall into the category of a Bravais lattice for which the surface can be generated by repeating the basic unit. Exceptions are surfaces of quasi-crystalline materials or with reconstruction. Assuming the surface is a 2D Bravais lattice, it can be generated by a pair of primitive vectors, $\mathbf{a}_1$, $\mathbf{a}_2$. Its reciprocal vectors $\mathbf{b}_1$, $\mathbf{b}_2$ can be calculated by

$$\mathbf{a}_i \cdot \mathbf{b}_j = \begin{cases} 2\pi & i = j \\ 0 & i \neq j \end{cases} \tag{35}$$

An approximation of the corrugation potential $U_c(x, y)$ is given by the first term of the 2D Fourier series of the primitive lattice vectors and has the form,

$$U_c(x, y) = U[\cos(\mathbf{b}_1 \cdot \mathbf{x}) + \cos(\mathbf{b}_2 \cdot \mathbf{x})], \tag{36}$$

where $\mathbf{x}$ is the vector of x and y positions.

For example, in the case of an FCC(100) surface such as that shown in Fig. 17a, the primitive vectors are

$$\mathbf{a}_1 = \begin{pmatrix} a \\ 0 \end{pmatrix}, \mathbf{a}_2 = \begin{pmatrix} 0 \\ a \end{pmatrix} \tag{37}$$

The corresponding reciprocal vectors are

$$\mathbf{b}_1 = \begin{pmatrix} \frac{2\pi}{a} \\ 0 \end{pmatrix}, \mathbf{b}_2 = \begin{pmatrix} 0 \\ \frac{2\pi}{a} \end{pmatrix}. \tag{38}$$

The corrugation potential can be formulated as,

$$U_c(x, y) = U\left[\cos\left(\frac{2\pi x}{a}\right) + \cos\left(\frac{2\pi y}{a}\right)\right] \tag{39}$$

and is illustrated in Fig. 17c

In another case, FCC(111), the surface is modeled as shown in Fig. 17b. According to the procedure we described above, one can chose two of the three lattice vectors, $\mathbf{a}_1$, $\mathbf{a}_2$, $\mathbf{a}_3$ as the primitive lattice vectors.

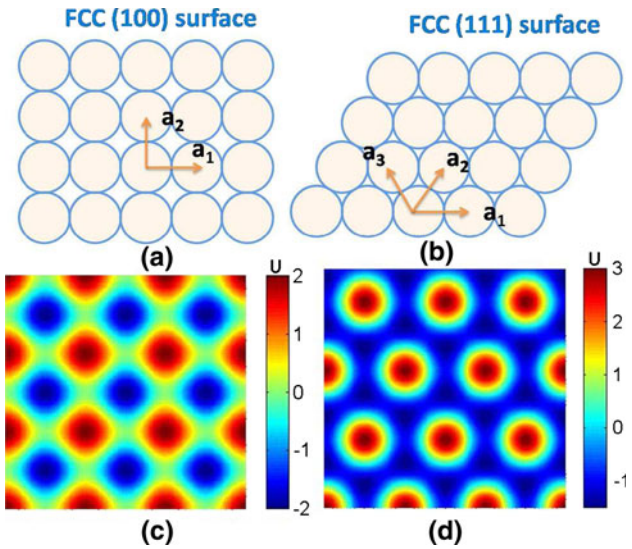

Fig. 17 Illustration of atom arrangements and energy landscapes on FCC(100) and FCC(111) surfaces. The energy unit is U which is the amplitude in Eqs. 39 and 46

$$\mathbf{a}_1 = \begin{pmatrix} a \\ 0 \end{pmatrix}, \mathbf{a}_2 = \begin{pmatrix} \frac{1}{2}a \\ \frac{\sqrt{3}}{2}a \end{pmatrix}, \mathbf{a}_3 = \begin{pmatrix} -\frac{1}{2}a \\ \frac{\sqrt{3}}{2}a \end{pmatrix} \quad (40)$$

If we choose a_1 and a_2, the reciprocal vectors are

$$\mathbf{b}_1 = \begin{pmatrix} \frac{2\pi}{a} \\ \frac{-2\pi}{\sqrt{3}a} \end{pmatrix}, \mathbf{b}_2 = \begin{pmatrix} 0 \\ \frac{4\pi}{\sqrt{3}a} \end{pmatrix}; \quad (41)$$

If we choose a_1 and a_3, the reciprocal vectors are,

$$\mathbf{b'}_1 = \begin{pmatrix} \frac{2\pi}{a} \\ \frac{2\pi}{\sqrt{3}a} \end{pmatrix}, \mathbf{b'}_3 = \begin{pmatrix} 0 \\ \frac{4\pi}{\sqrt{3}a} \end{pmatrix}; \quad (42)$$

If we choose a_2 and a_3, the reciprocal vectors are,

$$\mathbf{b''}_2 = \begin{pmatrix} \frac{2\pi}{a} \\ \frac{2\pi}{\sqrt{3}a} \end{pmatrix}, \mathbf{b''}_3 = \begin{pmatrix} \frac{-2\pi}{a} \\ \frac{2\pi}{\sqrt{3}a} \end{pmatrix}. \quad (43)$$

However, there is a complication in that, if we only use two of the three possible lattice vectors, it is impossible to maintain symmetry in all three directions at the same time. So, a practical alternative is to use all the reciprocal vectors. Actually, there are only three unique reciprocal vectors such that the corrugation potential becomes,

$$U_c(x,y) = U[\cos(\mathbf{b}_1 \cdot \mathbf{x}) + \cos(\mathbf{b}_2 \cdot \mathbf{x}) + \cos(\mathbf{b}_3 \cdot \mathbf{x})] \quad (44)$$

in which $\mathbf{b}_1$, $\mathbf{b}_2$, and $\mathbf{b}_3$ can be expressed as,

$$\mathbf{b}_1 = \begin{pmatrix} \frac{2\pi}{a} \\ \frac{2\pi}{\sqrt{3}a} \end{pmatrix}, \mathbf{b}_2 = \begin{pmatrix} 0 \\ \frac{4\pi}{\sqrt{3}a} \end{pmatrix}, \mathbf{b}_3 = \begin{pmatrix} \frac{2\pi}{a} \\ \frac{-2\pi}{\sqrt{3}a} \end{pmatrix}. \quad (45)$$

Finally, we have a simplified form,

$$U_c(x,y) = U\left[2\cos\left(\frac{2\pi x}{a}\right)\cos\left(\frac{2\pi y}{\sqrt{3}a}\right) + \cos\left(\frac{4\pi y}{\sqrt{3}a}\right)\right]. \quad (46)$$

A visual representation of the energy landscape is shown in Fig. 17d. Other surfaces with Bravais lattices can be constructed in a similar way.

One interesting and relevant case is graphene. Graphene's structure is similar to the FCC(111) surface except there is one atom missing in the center of the hexagonal primitive cell. However, the corrugation potential for graphene can be constructed using the same set of primitive lattice vectors. As a result, there is only a sign difference between their corrugation potentials [66].

8.2 Scan-Line Dependence

In this section, we apply the 2D PT model to study the scanning line dependence of friction. We take the FCC(111) surface as an example. For the 2D PT model, the Langevin equation becomes,

$$m\ddot{x} + m\mu\dot{x} = -\frac{\partial V(x,y,t)}{\partial x} + \xi_x(t) \quad (47)$$

$$m\ddot{y} + m\mu\dot{y} = -\frac{\partial V(x,y,t)}{\partial y} + \xi_y(t), \quad (48)$$

where $\xi(t)_x = \xi(t)\cos(\theta)$ and $\xi(t)_y = \xi(t)\sin(\theta)$, and θ is subject to uniform distribution $[0, 2\pi]$.

We suppose that the support drags the tip to slide along the [110] direction, but with different starting positions. As shown in Fig. 18, although the support scans along a straight line, the tip moves through a zigzag pattern due to the 2D energy landscape. Along different scanning lines, one also obtains distinct force traces. How far the tip's path deviates from a straight line is determined by ratio of the curvature of the corrugation potential and the lateral stiffness of the system, or $\eta = \frac{2\pi^2 U}{a^2 k}$. The larger the value of η, the further the tip's path from a straight line.

One consequence of the zigzag path is the loss of resolution of the lateral force images from AFM which are widely used to measure a surface landscape at the atomic scale. In an ideal situation, the force obtained would reflect the gradient of the corrugation potential exactly alongthe scan line such that the measurement is a perfect representation of the surface. However, this may not be the case if the path of the tip deviates from a straight line since the force obtained is due to the gradient of the corrugation

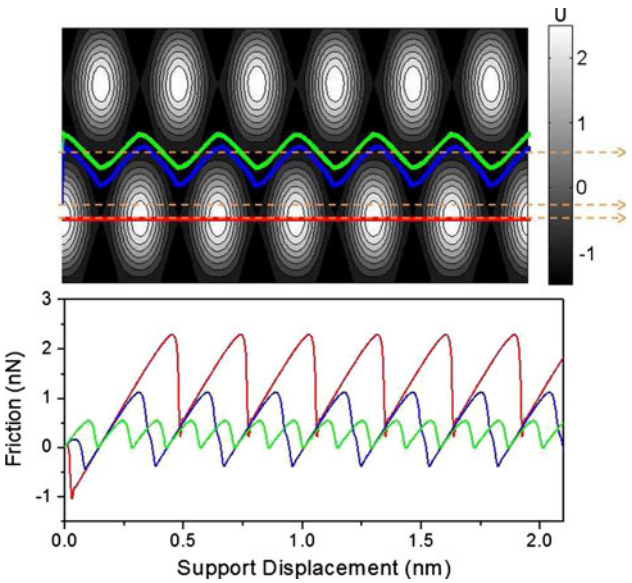

Fig. 18 Potential energy landscape of an FCC(111) surface (*top*) illustrating the position of the point tip (*solid lines*) traveling along different scan lines (*dashed lines*) and corresponding force traces (*bottom*). Results shown at $T = 0$ K to clearly illustrate the motion paths

potential where the tip resides. The favored positions for the tip are the minima in the energy landscape and, as a result, the information at the energy maxima is lost while the information at the minima is over-represented. Figure 19 exhibits lateral force images from a 2D PT model with varying system stiffness. The bright white represents high friction, and dark represents low friction. Larger values of k correspond to smaller η, and therefore less deviation from a straight path. Consistent with this expectation, the best resolution in Fig. 19 is observed with $k = 200$ N/s.

Similarly, we find that scanning in different directions causes the force patterns to differ due to the 2D nature of the energy landscape. Figure 20 shows the effect of scanning direction on both the tip's movement and friction with a FCC(111) where the tip moves at angles of 0°, 15°, and 30° relative to the [110] direction (the 0° scanning angle is the [110] direction). This surface has 60° periodicity due to its hexagonal structure so larger scanning angles can be mapped back to angles less than 60°; for example 75° is identical to 15°. At a scanning angle of 0° the tip takes a zigzag pattern which has also been observed in MD simulations [33, 68]. Further, for 0° and 30° the periodicity of the tip's movement is consistent with the periodicity of the corresponding force trace. Therefore, the 2D PT model can be used to predict the connection between the crystal structure, the path through which the tip moves and the frictional anisotropy. For example, friction anisotropy was observed on a quasicrystal surface [69] whose origin was then related to the crystallographic features of that surface [70]. There is potential for 2D PT-based models to reveal many more such relationships.

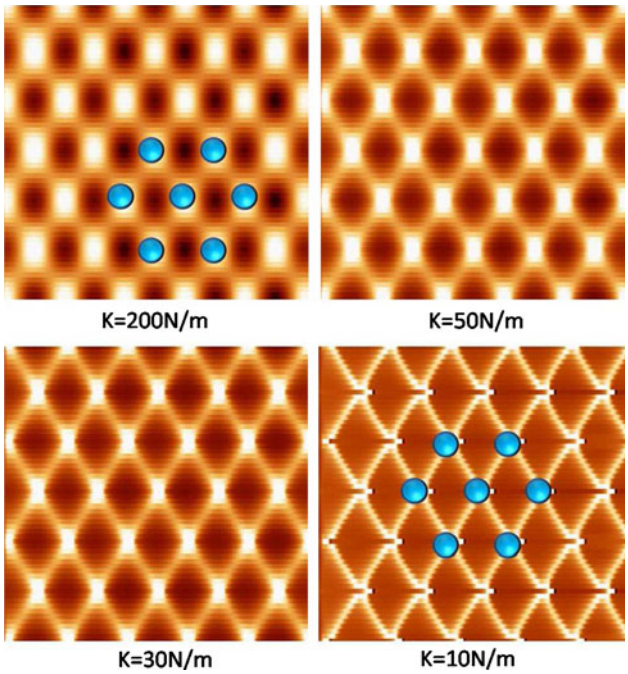

Fig. 19 Lateral force images of an FCC(111) surface for different system stiffness, k. *Blue spheres* identify the positions of atoms and show that the larger stiffness yields better the atomic resolution. Other model parameters: $m = 10^{-12}$ kg, $U = 0.6$ eV, $v = 4 \times 10^3$ nm/s, $\mu = \mu_c = 2\sqrt{k/m}$, lattice spacing in the [110] direction $a = 0.288$ nm

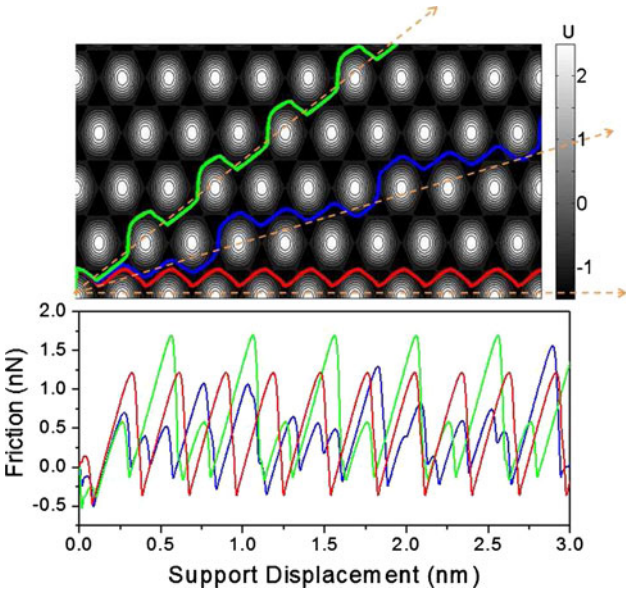

Fig. 20 Potential energy landscape of an FCC(111) surface (*top*) illustrating the position of the point tip (*solid lines*) as the support is moved in different directions from the same starting point (*dashed lines*), and corresponding force traces (*bottom*). Results shown at $T = 0$ K to clearly illustrate the motion paths

9 Contact Size and the FKT Model

So far, we have considered the tip to be concentrated at a single point-mass and a ball-like interaction between the tip and substrate. In reality, even for an atomically sharp tip, one cannot guarantee that the contact area contains only a single atom. It is usually assumed that multiple atoms at the end of the tip are involved in the interaction. However, the actual size of the contact during an experimental measurement is extremely difficult to directly measure. Therefore, the area dependence of friction is usually derived indirectly using the relationship between normal load and friction. Friction as a function of normal load can be obtained directly from experiment, but the relationship between contact area and normal load is usually estimated with contact mechanics [71], for example the Hertz [72], JKR [72], or DMT [73] models. Using normal load as the bridge between friction and area with the assumptions of continuum mechanics, the area dependence of friction is conventionally believed to be linear.

However, it is well known that continuum mechanics is valid only when the dimensions of the studied object are much larger than the length scale of the atomic discontinuity. Therefore, when the scale of the single asperity is on the order of nanometers, the effect of the discontinuity of the atoms within the tip and substrate can no longer be neglected [47]. Recent AFM experiments on metals revealed that friction varies little with increase of normal load in the low load regime [24, 74]. In addition, a newly invented AFM technique referred to as tip-on-top mode that enables researchers to manipulate nanoparticles of different size showed that in some cases friction increased linearly with interface area while in other cases near frictionless sliding was observed [75]. These conflicting results suggest that there may be a non-linear relationship between real contact area and friction.

The connection between contact area and friction on the atomic scale is therefore still not well understood and model-based prediction can provide insight into their fundamental connection. However, the reduced-order models we have discussed so far cannot capture the effect of a multi-atom contact area, so an extended model is needed to capture their combined effect. The FKT [6] model which combines the FK [5] and PT models has been proposed to account for the coupling between tip atoms. In the following sections, we describe implementation of 1D and 2D FKT models.

9.1 1D FKT

An illustration of the 1D FKT model is shown in Fig. 1 where adjacent tip atoms interact through harmonic springs k_t. The total potential energy of the system becomes,

$$V_{\mathrm{FKT}}(x,t) = \sum_{i=1}^{N} -\frac{1}{2}U\cos\left(\frac{2\pi x_i}{a}\right) + \sum_{i=1}^{N-1}\frac{k_t}{2}\left(\Delta x_{i,i+1} - b\right)^2 + \sum_{i=1}^{N}\frac{k}{2}\left(vt + (i-1)b - x_i\right)^2 \tag{49}$$

where N is the number of tip atoms, U is the amplitude of the sinusoidal corrugation potential, x_i is the displacement of the ith atom, a and b are respective substrate and tip lattice spacing, $\Delta x_{i,i+1}$ is the distance between atom i and adjacent atom $i+1$, v is the sliding speed of the support, and t is time. This expression includes the corrugation potential (the first term of Eq. 49), the potential resulting from the interaction between tip atoms via elastic springs k_t (second term), and the elastic potential due to tethering to the support by springs k (third term). The instantaneous friction force is then the sum of the force experienced by all the tip atoms,

$$F = \sum_{i=1}^{N} k(vt + (i-1)b - x_i). \tag{50}$$

An example implementation of the 1D FKT model is provided in the Supplementary Material as MATLAB program `FKT1D_RK.m`.

The FKT model can be used to predict the friction variation with the tip-substrate lattice mismatch b/a and the tip size N. Illustrative results are shown in Fig. 21. The first thing we notice is that only when $a = b$ does the friction increase linearly with the contact area. For other b/a, there exist some tip sizes where the friction significantly decreases. These so-called "magic sizes" [9] can be predicted. In the extreme case where we suppose $k_t = \infty$, the corrugation potential between the tip and substrate can be expressed as,

$$\begin{aligned} U_c &= -\frac{1}{2}U\sum_{i=1}^{N}\cos\left(\frac{2\pi(i-1)b + x}{a}\right) \\ &= -\frac{1}{2}U\frac{\sin(Nb\pi/a)}{\sin(b\pi/a)}\cos\left(\frac{\pi(Nb - b + 2x)}{a}\right). \end{aligned} \tag{51}$$

This means that the magnitude of the corrugation potential is zero when Nb/a is an integer. In this case, assuming there is no viscous term, the friction goes to zero. For example, for a lattice mismatch of $b/a = 4/5$, a minimum friction will occur at $N = 5$, 10, and so on.

Another observation is that, for any value of Nb/a, although the local friction minima arise only at some magic sizes, over a long range the friction increases linearly with the contact area [76]. The friction comes from the viscous force which is proportional to sliding speed. Physically speaking, the viscous term is due to phonon excitation. So the term "superlubricity" which suggests the complete

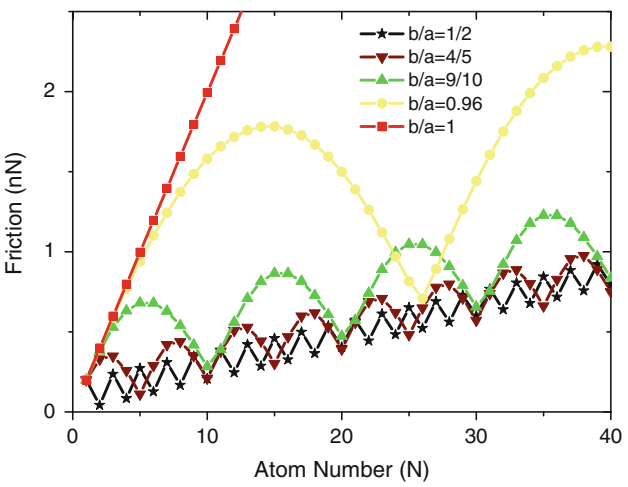

Fig. 21 Friction variation with the tip size N for different lattice mismatch b/a. $k = 5$ N/m and $k_t = 50$ N/m are used to obtain these results

cancelation of friction to zero may not be appropriate; structural lubricity proposed by Müser is a better term to describe the phenomenon [77].

9.2 2D FKT

Atomic friction and the tip size effect have been studied using the 1D FKT model since Weiss and Elmer's study [6]. However, there are now many experimental observations that cannot be captured by a 1D model. For example, increasing numbers of AFM measurements have shown that incommensurability due to misaligned surfaces can lead to very low friction [49, 78, 79]. To address these types of phenomena, we can extend the 1D FKT model to 2D [80, 81]. Figure 22 illustrates a representative setup for the 2D FKT model.

One effect we can study using this model is the misfit angle dependence of friction. We again use materials with FCC structure as an example. Both the tip and substrate contact interfaces are chosen as FCC(111) surfaces with identical lattice spacing $a = b = 0.288$ nm. Figure 23 shows that, for all contact sizes N, the friction reaches a maximum value at aligned angles, $i \times 60°$, where i is an integer. Once the system deviates from perfect commensurability, the friction force decreases significantly. Similar phenomena have been observed experimentally for contact between graphite surfaces [49, 66].

It has also been reported that incommensurate contact may result in intermediate states [82–84], and that the formation of intermediate states can lead to new mechanisms of energy dissipation and thus the breakdown of

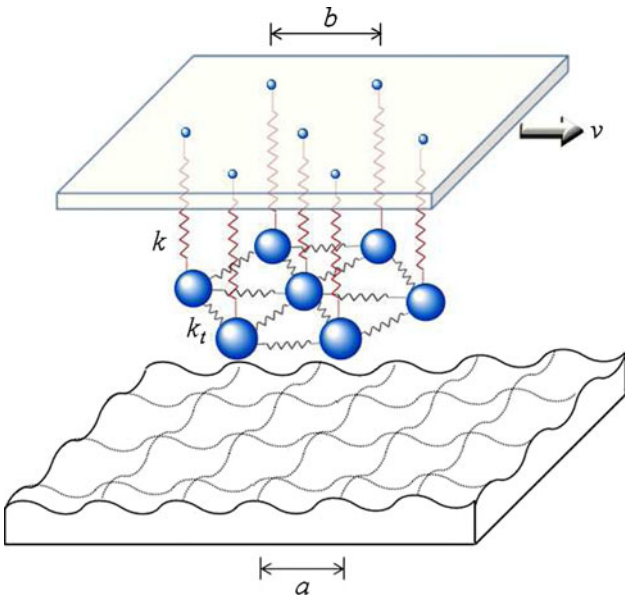

Fig. 22 2D FKT model where the tip atoms (*large spheres*) are connected to each other and to the support by harmonic springs

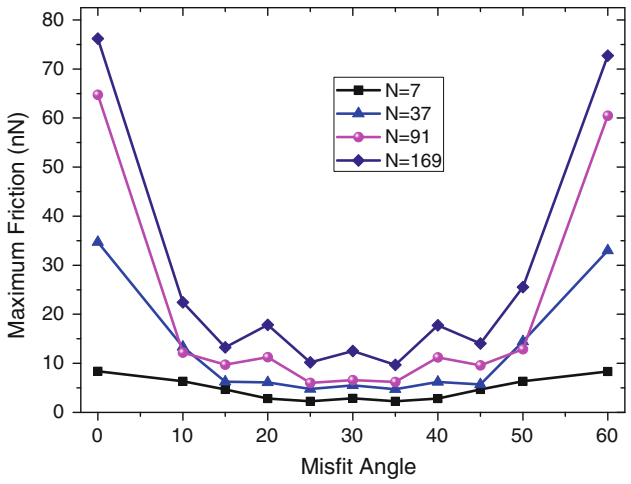

Fig. 23 The misfit angle dependence of friction with different tip sizes; $k_t = 50$ N/m and $k = 10$ N/m. The $N = 7$ curve corresponds to the model illustrated in Fig. 22

structural lubricity [77]. To study such effects using the 2D FKT model we need to define physically meaningful model parameters. For example, it is necessary to define the stiffness (captured in the model by k and k_t), and the strength of the interaction between tip and substrate (U in the model), since these properties ultimately determine the appearance of intermediate states and the occurrence of plastic deformation and wear in a real system. A thorough study of the effects of these properties will require collaborative work involving experiments, atomistic simulations, and reduced-order models.

10 Conclusions

Finally, we want to discuss the shortcomings of PT-based models for studying atomic friction. First, as a reduced-order model, the substrate is assumed to be a rigid body and the corrugation potential between the tip and substrate taken to have a sinusoidal form. Because of this, only elastic deformation is considered in the model. However, plastic deformation or wear may occur depending on materials, environment, normal load or other factors. Second, energy dissipation is added to the equation through a viscous term, $-m\mu\dot{x}$, such that the viscous term is the only channel through which energy can dissipate. However, in reality, energy is dissipated through electron conduction and phonon interaction. Taking phonon interaction as an example, there are many vibration modes ($3N$ where N is the number of atoms) and thus many energy dissipation channels the tip can turn to. Like thermal activation, the transition rate derived from a system with only one vibration mode may be substantially different from that derived from a system with many modes [38]. Third, many

interpretations of experimental phenomena through reduced-order modeling are on the phenomenological level; for example, friction modulation due to surface reconstruction [57], and formation and rupture of multiple contacts due to thermal effects [30]. These types of model-predicted mechanisms require validation and clarification from other methods such as direct experimental observation or fully atomistic modeling. Finally, given that the AFM cantilever itself has many eigenmodes [85] and the tip apex behaves differently still, it is not understood exactly how the reduced-order model can correctly capture the dynamics of the system. As shown in this and many other articles, even the simplest PT model is able to describe some of the behaviors of a complicated and multidimensional AFM experiment. While, this is fortunate for the research community, there are open questions regarding exactly why it works.

Despite the shortcomings of PT-based models, they play a significant and important role in facilitating qualitative understanding of the mechanisms of atomic friction. As shown in this article, they can be successfully used to predict a wide range of frictional phenomena, from the effects of temperature and speed to the role of contact area and commensurability. Although, some topics were only briefly discussed, the extensive reference list provided can be used to fill in the details on any individual topic. Overall, we hope this article acts as an introductory manual for newcomers to the field, as well as an illustration of the significant potential for this approach that will inspire others to continue its development and gain new insights into atomic-scale friction.

Acknowledgments We are grateful for insightful discussions with Drs. Qunyang Li and Danny Perez. This study was funded by the National Science Foundation through grant CMMI-1068552.

References

1. Szlufarska, I., Chandross, M., Carpick, R.W.: Recent advances in single-asperity nanotribology. J. Phys. D Appl. Phys. **41**, 123001 (2008)
2. Prandtl, L.: Hypothetical model for the kinetic theory of solid bodies. Z. Angew. Math. Mech. **8**, 85–106 (1928)
3. Tomlinson, G.: A molecular theory of friction. Philos. Mag. **7**, 905 (1929)
4. Gnecco, E., Bennewitz, R., Loppacher, C., Bammerlin, M., Meyer, E., Guntherodt, H.-J.: Velocity dependence of atomic friction. Phys. Rev. Lett. **84**, 1172 (2000)
5. Kontorova, T., Frenkel, Yu.I.: On the theory of plastic deformation. Zh. Exp. Teor. Fiz. **8**, 1340–1344 (1938)
6. Weiss, M., Elmer, F.: Dry friction in the Frenkel–Kontorova–Tomlinson model: static properties. Phys. Rev. B **53**, 7539 (1996)
7. Sang, Y., Dube, M., Grant, M.: Thermal effects on atomic friction. Phys. Rev. Lett. **87**, 174301 (2001)
8. Fusco, C., Fasolino, A.: Velocity dependence of atomic-scale friction: a comparative study of the one- and two-dimensional Tomlinson model. Phys. Rev. B **71**, 045413 (2005)
9. Igarashi, M., Natori, A., Nakamura, J.: Size effects in friction of multiatomic sliding contacts. Phys. Rev. B **78**, 165427 (2008)
10. Steiner, P., Roth, R., Gnecco, E., Baratoff, A., Maier, S., Glatzel, T., Meyer, E.: Two-dimensional simulation of superlubricity on NaCl and highly oriented pyrolytic graphite. Phys. Rev. B **79**, 045414 (2009)
11. Krylov, S.Y., Frenken, J.W.M.: Thermal contact delocalization in atomic scale friction: a multitude of friction regimes. New J. Phys. **9**, 398 (2007)
12. Furlong, O., Manzi, S., Pereyra, V., Bustos, V., Tysoe, W.T.: Kinetic Monte Carlo theory of sliding friction. Phys. Rev. B **80**, 153408 (2009)
13. Allen, M.P., Tildesley, D.J.: Computer Simulation of Liquids. Oxford University Press, Oxford (1987)
14. Ermak, D., Buckholz, H.: Numerical integration of the Langevin equation: Monte Carlo simulation. J. Comp. Phys. **35**, 169 (1980)
15. Nakamura, J., Wakunami, S., Natori, A.: Double-slip mechanism in atomic-scale friction: Tomlinson model at finite temperatures. Phys. Rev. B **72**, 235415 (2005)
16. Iizuka, H., Nakamura, J., Natori, A.: Control mechanism of friction by dynamic actuation of nanometer-sized contacts. Phys. Rev. B **80**, 155449 (2009)
17. Brańka, A., Heyes, D.: Algorithms for Brownian dynamics simulation. Phys. Rev. E **58**, 2611–2615 (1998)
18. Honeycutt, R.: Stochastic Runge–Kutta algorithms. I. White noise. Phys. Rev. A **45**, 600–603 (1992)
19. Kasdin, N.: Runge–Kutta algorithm for the numerical integration of stochastic differential equations. J. Guid. Control Dyn. **18**, 114 (1995)
20. Higham, D.: An algorithmic introduction to numerical simulation of stochastic differential equations. SIAM Rev. **43**, 525–546 (2001)
21. Jansen, L., Hölscher, H., Fuchs, H., Schirmeisen, A.: Temperature dependence of atomic-scale stick-slip friction. Phys. Rev. Lett. **104**, 256101 (2010)
22. Bennewitz, R., Gyalog, T., Guggisberg, M., Bammerlin, M., Meyer, E., Güntherodt, H.J.: Atomic-scale stick-slip processes on Cu(111). Phys. Rev. B **60**, R11301 (1999)
23. Riedo, E., Gnecco, E., Bennewitz, R., Meyer, E., Brune, H.: Interaction potential and hopping dynamics governing sliding friction. Phys. Rev. Lett. **91**, 084502 (2003)
24. Li, Q., Dong, Y., Perez, D., Martini, A., Carpick, R.W.: Speed dependence of atomic stick-slip friction in optimally matched experiments and molecular dynamics simulations. Phys. Rev. Lett. **106**, 126101 (2011)
25. Furlong, O., Manzi, S., Pereyra, V., Bustos, V., Tysoe, W.: Monte Carlo simulations for Tomlinson sliding models for non-sinusoidal periodic potentials. Tribol. Lett. **39**, 177 (2010)
26. Krylov, S.Y., Jinesh, K.B., Valk, H., Dienwiebel, M., Frenken, J.W.M.: Thermally induced suppression of friction at the atomic scale. Phys. Rev. E **71**, 065101 (2005)
27. Jinesh, K.B., Krylov, S.Y., Valk, H., Dienwiebel, M., Frenken, J.W.M.: Thermolubricity in atomic-scale friction. Phys. Rev. B **78**, 155440 (2008)
28. Zhao, X., Phillpot, S.R., Sawyer, W.G., Sinnott, S., Perry, S.: Transition from thermal to athermal friction under cryogenic conditions. Phys. Rev. Lett. **102**, 186102 (2009)
29. Schirmeisen, A., Jansen, L., Holscher, H., Fuchs, H.: Temperature dependence of point contact friction on silicon. Appl. Phys. Lett. **88**, 123108 (2006)
30. Barel, I., Urbakh, M., Jansen, L., Schirmeisen, A.: Multibond dynamics of nanoscale friction: the role of temperature. Phys. Rev. Lett. **104**, 66104 (2010)

31. Barel, I., Urbakh, M., Jansen, L., Schirmeisen, A.: Temperature dependence of friction at the nanoscale: when the unexpected turns normal. Tribol. Lett. **39**, 311–319 (2010)
32. Müser, M.: Nature of mechanical instabilities and their effect on kinetic friction. Phys. Rev. Lett. **89**, 224301 (2002)
33. Dong, Y., Perez, D., Voter, A., Martini, A.: The roles of statics and dynamics in determining transitions between atomic friction regimes. Tribol. Lett. **42**, 99–107 (2011)
34. Chen, J., Ratera, I., Park, J., Salmeron, M.: Velocity dependence of friction and hydrogen bonding effects. Phys. Rev. Lett. **96**, 236102 (2006)
35. Evstigneev, M., Reimann, P.: Refined force-velocity relation in atomic friction experiments. Phys. Rev. B **73**, 113401 (2006)
36. Reimann, P., Evstigneev, M.: Nonmonotonic velocity dependence of atomic friction. Phys. Rev. lett. **93**, 230802 (2004)
37. Granato, E., Ying, S.: Non-monotonic velocity dependence of atomic friction. Tribol. Lett. **39**, 229–233 (2010)
38. Hänggi, P., Talkner, P., Borkovec, M.: Reaction-rate theory: fifty years after Kramers. Rev. Mod. Phys. **62**, 251 (1990)
39. Krylov, S.Y., Dijksman, J.A., van Loo, W.A., Frenken, J.W.M.: Stick-slip motion in spite of a slippery contact: do we get what we see in atomic friction?. Phys. Rev. Lett. **97**, 166103 (2006)
40. Tshiprut, Z., Filippov, A., Urbakh, M.: Effect of tip flexibility on stick-slip motion in friction force microscopy experiments. J. Phys. Condens. Matter **20**, 354002 (2008)
41. Lu, P., Loke, Y., Tang, X., Kushvaha, S., OShea, S.: A note on the two-spring Tomlinson model. Tribol. Lett. **43**, 73 (2011)
42. Conley, W., Krousgrill, C., Raman, A.: Stick-slip motions in the friction force microscope: effects of tip compliance. Tribol. Lett. **29**, 23–32 (2008)
43. Conley, W., Raman, A., Krousgrill, C.: Nonlinear dynamics in Tomlinsons model for atomic-scale friction and friction force microscopy. J. Appl. Phys. **98**, 053519 (2005)
44. Johnson, K., Woodhouse, J.: Stick slip motion in the atomic force microscope. Tribol. Lett. **5**, 155–160 (1998)
45. Medyanik, S., Liu, W., Sung, I.H., Carpick, R.W.: Predictions and observations of multiple slip modes in atomic-scale friction. Phys. Rev. Lett. **97**, 136106 (2006)
46. Roth, R., Glatzel, T., Steiner, P., Gnecco, E., Baratoff, A., Meyer, E.: Multiple slips in atomic-scale friction: an indicator for the lateral contact damping. Tribol. Lett. **39**, 63–69 (2010)
47. Luan, B., Robbins, M.: The breakdown of continuum models for mechanical contacts. Nat. Biotechnol. **435**, 929–932 (2005)
48. Socoliuc, A., Bennewitz, R., Gnecco, E., Meyer, E.: Transition from stick-slip to continuous sliding in atomic friction: entering a new regime of ultralow friction. Phys. Rev. Lett. **92**, 134301 (2004)
49. Dienwiebel, M., Verhoeven, G., Pradeep, N., Frenken, J.: Superlubricity of graphite. Phys. Rev. Lett. **92**, 126101 (2004)
50. Harten, U., Lahee, A.M., Toennies, J.P., Wöll, C.: Observation of a soliton reconstruction of Au(111) by high-resolution helium-atom diffraction. Phys. Rev. Lett. **54**, 2619–2622 (1985)
51. Wöll, C., Chiang, S., Wilson, R.J., Lippel, P.H.: Determination of atom positions at stacking-fault dislocations on Au(111) by scanning tunneling microscopy. Phys. Rev. B **39**, 7988–7991 (1989)
52. Maier, S., Gnecco, E., Baratoff, A., Bennewitz, R., Meyer, E.: Atomic-scale friction modulated by a buried interface: combined atomic and friction force microscopy experiments. Phys. Rev. B **78**, 45432 (2008)
53. Filleter, T., Bennewitz, R.: Structural and frictional properties of graphene films on SiC(0001) studied by atomic force microscopy. Phys. Rev. B **81**, 155412 (2010)
54. Tshiprut, Z., Zelner, S., Urbakh, M.: Temperature-induced enhancement of nanoscale friction. Phys. Rev. Lett. **102**, 136102 (2009)
55. Fajardo, O.Y., Mazo, J.J.: Effects of surface disorder and temperature on atomic friction. Phys. Rev. B **82**, 035435 (2010)
56. Motchongom-Tingue, M., Djuidjé Kenmoé, G., Kofané, T.: Stick-slip motion and static friction in a nonlinear deformable substrate potential. Tribol. Lett. **43**, 65 (2011)
57. Steiner, P., Gnecco, E., Filleter, T., Gosvami, N., Maier, S., Meyer, E., Bennewitz, R.: Atomic friction investigations on ordered superstructures. Tribol. Lett. **39**, 321 (2010)
58. Li, Q., Dong, Y., Martini, A., Carpick, R.W.: Atomic friction modulation on the reconstructed Au (111) surface. Tribol. Lett. **3**, 369 (2011)
59. Socoliuc, A., Gnecco, E., Maier, S., Pfeiffer, O., Baratoff, A., Bennewitz, R., Meyer, E.: Atomic-scale control of friction by actuation of nanometer-sized contacts. Science **313**, 207 (2006)
60. Lantz, M., Wiesmann, D., Gotsmann, B.: Dynamic superlubricity and the elimination of wear on the nanoscale. Nat. Nanotechnol. **4**, 586–591 (2009)
61. Maier, S., Sang, Y., Filleter, T., Grant, M., Bennewitz, R., Gnecco, E., Meyer, E.: Fluctuations and jump dynamics in atomic friction experiments. Phys. Rev. B **72**, 245418 (2005)
62. Igarashi, M., Nakamura, J., Natori, A.: Mechanism of velocity saturation of atomic friction force and dynamic superlubricity at torsional resonance. Jpn. J. Appl. Phys. **46**, 5591 (2007)
63. Fujisawa, S., Sugawara, Y., Ito, S., Mishima, S., Okada, T., Morita, S.: The two-dimensional stick-slip phenomenon with atomic resolution. Nanotechnology **4**, 138 (1993)
64. Fujisawa, S., Kishi, E., Sugawara, Y., Morita, S.: Atomic-scale friction observed with a two-dimensional frictional-force microscope. Phys. Rev. B **51**, 7849–7857 (1995)
65. Kerssemakers, J., De Hosson, J.: Atomic force microscopy imaging of transition metal layered compounds: a two-dimensional stick-slip system. Appl. Phys. Lett. **67**, 347 (1995)
66. Verhoeven, G., Dienwiebel, M., Frenken, J.: Model calculations of superlubricity of graphite. Phys. Rev. B **70**, 165418 (2004)
67. Steiner, P., Roth, R., Gnecco, E., Baratoff, A., Meyer, E.: Angular dependence of static and kinetic friction on alkali halide surfaces. Phys. Rev. B **82**, 205417 (2010)
68. Sörensen, M.R., Jacobsen, K.W., Stoltze, P.: Simulations of atomic-scale sliding friction. Phys. Rev. B **53**, 2101–2113 (1996)
69. Park, J., Ogletree, D., Salmeron, M., Ribeiro, R., Canfield, P., Jenks, C., Thiel, P.: High frictional anisotropy of periodic and aperiodic directions on a quasicrystal surface. Science **309**, 1354 (2005)
70. Filippov, A., Vanossi, A., Urbakh, M.: Origin of friction anisotropy on a quasicrystal surface. Phys. Rev. lett. **104**, 74302 (2010)
71. Johnson, K.: Mechanics of adhesion. Tribol. Int. **31**, 413–418 (1998)
72. Johnson, K., Kendall, K., Roberts, A.: Surface energy and the contact of elastic solids. Proc. R. Soc. Lond. Ser. A **324**, 301–313 (1971)
73. Derjaguin, B., Muller, V., Toporov, Y.: Effect of contact deformations on the adhesion of particles. J. Colloid Interface Sci. **67**, 314–326 (1975)
74. Gosvami, N., Filleter, T., Egberts, P., Bennewitz, R.: Microscopic friction studies on metal surfaces. Tribol. Lett. **39**, 19–24 (2010)
75. Dietzel, D., Ritter, C., Monninghoff, T., Fuchs, H., Schirmeisen, A., Schwarz, U.: Frictional duality observed during nanoparticle sliding. Phys. Rev. Lett. **101**, 125505 (2008)
76. Dong, Y., Li, Q., Wu, J., Martini, A.: Friction, slip and structural inhomogeneity of the buried interface. Model. Simul. Mater. Sci. Eng. **19**, 065003 (2011)
77. Müser, M.: Structural lubricity: role of dimension and symmetry. Europhys. Lett. **66**, 97–103 (2004)
78. Hirano, M., Shinjo, K., Kaneko, R., Murata, Y.: Anisotropy of frictional forces in muscovite mica. Phys. Rev. Lett. **67**, 2642–2645 (1991)

79. Crossley, A., Kisi, E.H., Summers, J.W.B., Myhra, S.: Ultra-low friction for a layered carbide-derived ceramic, Ti_3SiC_2, investigated by lateral force microscopy (LFM). J. Phys. D Appl. Phys. **32**, 632 (1999)
80. Gyalog, T., Bammerlin, M., Lüthi, R., Meyer, E., Thomas, H.: Mechanism of atomic friction. Europhys. Lett. **31**, 269 (1995)
81. Gyalog, T., Thomas, H.: Friction between atomically flat surfaces. Europhys. Lett. **37**, 195 (1997)
82. Kim, W., Falk, M.: Atomic-scale simulations on the sliding of incommensurate surfaces: the breakdown of superlubricity. Phys. Rev. B **80**, 235428 (2009)
83. Braun, O., Manini, N.: Dependence of boundary lubrication on the misfit angle between the sliding surfaces. Phys. Rev. E **83**, 021601 (2011)
84. Manini, N., Braun, O.: Crystalline misfit-angle implications for solid sliding. Phys. Lett. A **375**, 2946. Arxiv preprint arXiv:11015508 (2011)
85. Raman, A., Melcher, J., Tung, R.: Cantilever dynamics in atomic force microscopy. Nano Today **3**, 20–27 (2008)